Catalysis Today 400-401 (2022) 35–48

Contents lists available at ScienceDirect

Catalysis Today

journal homepage: www.elsevier.com/locate/cattod

Hydrogen and value-added liquid fuel generation from pyrolysis-catalytic steam reforming conditions of microplastics waste dissolved in phenol over bifunctional Ni-Pt supported on Ti-Al nanocatalysts

Walid Nabgan, PhD [a,b,*], Bahador Nabgan, PhD [a,b], Tuan Amran Tuan Abdullah [a,b,*], Muhammad Ikram [c,**], Arvind H. Jadhav [d], Mohamad Wijayanuddin Ali [a,b], Aishah Abdul Jalil [a,b]

[a] School of Chemical and Energy Engineering, Faculty of Engineering, Universiti Teknologi Malaysia, 81310 Skudai, Johor, Malaysia
[b] Centre of Hydrogen Energy, Institute of Future Energy, Universiti Teknologi Malaysia, 81310 Skudai, Johor, Malaysia
[c] Solar Cell Applications Research Lab, Department of Physics, Government College University Lahore, 54000, Punjab, Pakistan
[d] Centre for Nano and Material Science, JAIN University, Jain Global Campus, Bangalore 562112, Karnataka, India

ARTICLE INFO

Keywords:
Hydrogen
Microplastics
Phenol
Pyrolysis-catalytic
Nano-catalysts

ABSTRACT

This research looks at the potential of utilizing microplastics waste (MPW) found in oceans and soil as a source of liquid fuel. A significant portion of this pollutant is presently untreated and ends up in landfills, exacerbating the worldwide issue of marine and land pollution. Pyrolysis is a tertiary recycling process that is presented as a solution in the presence of a catalyst. This study aimed to develop bifunctional Ni-Pt nanocatalysts supported on TiO_2 and Al_2O_3 for hydrogen and valued fuels generation from pyrolysis-catalytic steam reforming conditions of microplastics waste dissolved in phenol. The chemical and physical properties of nanocatalysts were characterized by BET, XRD, TEM, FESEM, FTIR, H_2-TPR, CO_2-TPD, NH_3-TPD, TGA, ICP and CHNS. It was found that the introduction of a small portion of Pt (2 wt%) metal to the Ni/Ti-Al nanocatalyst was found to significantly enhance the reducibility, acidity, basicity nanocatalyst performance and stability. C–O(H), C═C–C, and C–O were the major functional clusters of the liquid yields surveyed from the FTIR spectrums during pyrolysis. A valuable liquid product such as trimethyl-(2-trimethylsilylphenyl)silane, cyclohexane-1,3-dione, 2-allylamino-methylene-5,5-dimethyl-, bis(2-ethylhexyl)phthalate (BEHP), etc. compounds were produced from the pyrolysis-catalytic steam reforming reaction. This sight is a crucial indication of utilizing microplastics pollution for value-added fuel production and decreasing the risk threats of marine life.

1. Introduction

Sustainable waste management is a crucial part of environmental preservation, and one of the most challenging forms of pollution to handle is plastic. One of the most dangerous plastic wastes to the marine and soil is micro-plastic waste with an element size lower than 5 mm. This sort of waste is produced through photo and thermo-oxidative degradation when exposed to environmental conditions. Researchers, regulatory agencies, and the general public are increasingly concerned about the abundance of microplastic waste (MPW) in the marine environment, both locally and worldwide. Microplastics in the seas have been thought to be potentially harmful and may negatively impact creatures across the food chain, although the ecological and public health implications of microplastics have not yet to be completely understood. Microplastics have been proven to damage aquatic creatures, as well as turtles and birds, in the following ways: they block digestive tracts, reduce the urge to eat, and change feeding behavior, all of which decrease development and reproductive output, according to the National Geographic Society. As a consequence of their intestines being stuffed with plastic, some animals suffer and die. Several studies have shown that microplastic causes metabolic abnormalities, neurotoxicity, and an elevated risk of cancer disease [1]. One of the proposed methods

* Corresponding authors at: School of Chemical and Energy Engineering, Faculty of Engineering, Universiti Teknologi Malaysia, 81310 Skudai, Johor, Malaysia.
** Corresponding author.
E-mail addresses: wnabgan@gmail.com (W. Nabgan), bnkabi62@yahoo.com (B. Nabgan), tamran@cheme.utm.my (T.A. Tuan Abdullah), dr.muhammadikram@gcu.edu.pk (M. Ikram).

https://doi.org/10.1016/j.cattod.2021.11.026
Received 26 June 2021; Received in revised form 12 September 2021; Accepted 14 November 2021
Available online 23 November 2021

to eco-friendly utilizes these plastic wastes is melting plastic with proper chemicals such as phenol and use it as feed for catalytic reforming and cracking reactions. This idea not only solves the disposal issue of microplastics into oceans and soils but result in hydrogen and syngas production and valuable liquid fuels generations as well [2–4]. In addition, phenolic compounds are commonly discharged from coal chemical mills, pharmaceutical manufacturers, oil refineries, and phenolic resin synthesis facilities. They are among the most prevalent harmful contaminants in wastewater [5]. Phenols are also one of the main components of bio-oil that could be suitable sources for hydrogen generation in the future [3,6,7]. Thus, the utilization of microplastics and phenol deliver a great idea for waste recycling as well as renewable and clean energy production for harmful resources. New nano-sized catalysts suited to convert these feedstocks with high conversion rates, selectivities, and stabilities are required to develop such processes for the manufacture of chemicals and fuels from microplastics and phenol cracking and reforming reactions.

The employment of reforming nanocatalysts with high activity at low temperatures while also suppressing coke formation reactions is an essential aspect of such an integrated system for hydrogen generation. The nanocatalysts in the catalytic reaction of steam reforming mainly have two influences. The first is to encourage the breakage of the O–H, C–C, and C–H bonds in the reactant molecules, resulting in small sections that are subsequently reconnected to yield gas products such as H_2, CO_2, and CO. The second option is to alter the reaction pathways of side reactions such phenol steam reforming ($C_6H_5OH + 5H_2O \rightarrow 6CO + 8H_2$, $\Delta H^\circ = 710.91$ kJ/mol) and water gas shift reactions ($CO + H_2O \leftrightarrow CO_2 + H_2$, $\Delta H^\circ = -41$ kJ/mol). Ni is widely used in the steam reforming reaction manufacturing scale because of its high performance, cheap cost, abundant availability, and strong catalytic activity toward the shattering of C–C and C–H bonds [8]. However, one of the most significant obstacles to steam reforming is the enormous thermodynamic potential for coke production. As a result, efforts should be focused on developing a high-activity, stable Ni-based catalyst with low Ni sintering and carbon formation; thus, the use of multi/bi-metals has grown in popularity because metals synthesized together improve catalytic performance [9]. It has been extensively stated that Ni-based bimetallic catalytic samples synthesized by adding guest metals like Ru, Pd, and Pt might alter Ni dispersion, reduce deposited carbon, improve thermal stability, and boost activity [10–14]. In addition, since bimetallic catalysts frequently outperform their parent metals with distinct features, doping precious metal on Ni-based catalysts should give an alternate option [15]. Among noble metals, platinum (Pt) displays high catalytic performance because the phenoxy types are known to be intensely accumulated on Pt(1 1 1) by the aromatics ring [16]. Juntian and coworkers [17] synthesized 1.0Pt–12Ni/Mg-Al catalysts for the methane dry reforming reaction. The kinetic study of their research showed that bimetallic 1.0Pt–12Ni catalyst enhanced the catalytic activity of the catalyst by decreasing the activation energy for CH_4 dissociation, lowering the energy barrier for CO_2 activation, and promotes the formation of surface O* by CO_2 adsorptive dissociation. Anand et al. [18] prepared bimetallic Pt (1.2 wt%)–Ni (0.4 wt%) over γ-alumina catalyst for hydrogen generation from catalytic reforming of pure glycerol. They found that this catalyst was stable for 85 h of the experimental test. Bimetallic Ni–Pt was used for the dry reforming of methane [19,20]. They mentioned that introducing Pt into Ni metal resulted in higher Ni reducibility and prevented coke formation on the catalyst surface, which then casing an enhancement in the catalytic performance.

It is generally recognized that the metal type and the support may influence the qualities of an ideal reforming catalyst. Although carbon production may be controlled by utilizing appropriate supports, supporting materials greatly enhance catalyst performance [21]. Titanium dioxide (TiO_2) has gotten a lot of consideration in the recent decade because of its twin functions as reducible support and an active metal [22]. Therefore, TiO_2 support delivers unique electronic interactions between the metal and the support [23]. However, it has low mechanical strength and low specific surface, and at high temperatures, it undergoes a phase shift from anatase to rutile, making it unsuitable for high-temperature processes [24]. One possible solution for this issue is incorporating TiO_2 with other metal oxides such as Aluminum oxide (Al_2O_3). Al_2O_3 possesses properties such as excellent metal dispersion because of its large surface area, cost-effectiveness, chemical, and mechanical steadiness and is one of the most often utilized supports [25]. Sadeq et al. [26] stated that incorporating TiO_2 into Al_2O_3 supports might help with metal dispersion, particle sintering, thermal stability, and oxygen storage capability, which aid in the gasification of carbon generated during the reforming process. Thus, TiO_2 into Al_2O_3 was chosen to support the bimetallic Ni–Pt nanocatalyst in this study.

In addition to developing suitable nanocatalyst, the preparation technique is also an essential matter to synthesize nanocatalysts with high activity and stability in the reforming process. Our previous studies [2,4] found hydrothermal treatment greatly affects the catalytic cracking and steam reforming reaction of phenol dissolved in polyethylene terephthalate plastic waste. However, to our knowledge, there is a lack of studies on nanocatalyst development in phenol and microplastics steam reforming and pyrolysis reaction for hydrogen and liquid fuel generation. We have prepared Ni-Pt/Al nano-sized catalyst supported on TNPs, but with a fixed ratio of Ni to Pt metals, for hydrogen and liquid fuel production from polyethylene terephthalate plastic waste dissolved in phenol [3]. Hence, this study investigates the influence of different volume ratios of bimetallic and monometallic Ni and Pt catalysts supported on the Al-Ti for steam reforming and pyrolysis reactions of microplastics-phenol to generate hydrogen and valued liquid fuel. Characterization of nanocatalysts is an essential stage in catalytic research since it allows researchers to look into important elements of nanocatalyst structure, surface characteristics, and activity. Nano-sized catalysts were synthesized through hydrothermal treatment method and characterized via TEM, FTIR, BET, XRD, FESEM, NH_3–TPD, CO_2–TPD, H_2–TPR, and ICP test. Prepared samples were screened at 500 °C, and the best nanocatalyst was tested at the temperature range of 500 °C to 700 °C. The nanocatalyst stability was also investigated in the three days on stream. Finally, Gas products were analyzed by GC–TCD, and liquid products were analyzed by GC–FID, GC/MS, and FTIR, and used nanocatalysts were characterized again via BET, ICP, TGA, and CHNS.

2. Materials and methods

2.1. Preparation of Ni-Pt/Ti-Al nano-catalysts

The typical procedures for preparing Ni-Pt/Ti-Al nanocatalysts are mainly hydrothermal treatment, impregnation, and reduction reactions. The starting substances such as nickel nitrate ($Ni(NO_3)_2.6\ H_2O$), platinum, titanium dioxide (TiO_2), alpha-alumina (γ-Al_2O_3), and NaOH were bought from Sigma-Aldrich and employed without additional purification. Generally, 45 wt% of each metal oxide (45 wt% of Ti or 45 wt % of Al) were gently added to 70 mL of deionized water while stirring at room temperature. NaOH pellets with the molar ratio to the support of 4:1 were then added into the solution and stirred for an hour. The support solution was transferred into an autoclave reactor equipped with 100 mL of Teflon cylinder, sealed, and kept into a furnace at 140 °C for 48 h. Those autoclave reactors were then cooled down at room temperature, and prepared liquid samples were filtered and washed with deionized water 18 times, then dried overnight at 110 °C. The prepared white samples were calcined at 800 °C for four hours. Those two prepared powders were then added into 150 mL of stirred deionized water. While stirring at 90 °C, Ni and Pt metals with different ratios were impregnated with the support until some water vaporized and homogenous solution volume decreased to 90 mL. Again, this solution was transferred into an autoclave reactor, heated at 140 °C for 48 h, filtered, washed, dried at 110 °C, and calcined at 800 °C. The ratios of metals (10 wt% in total) over 90 wt% of supports were 10% Ni (named as Ni), 8%

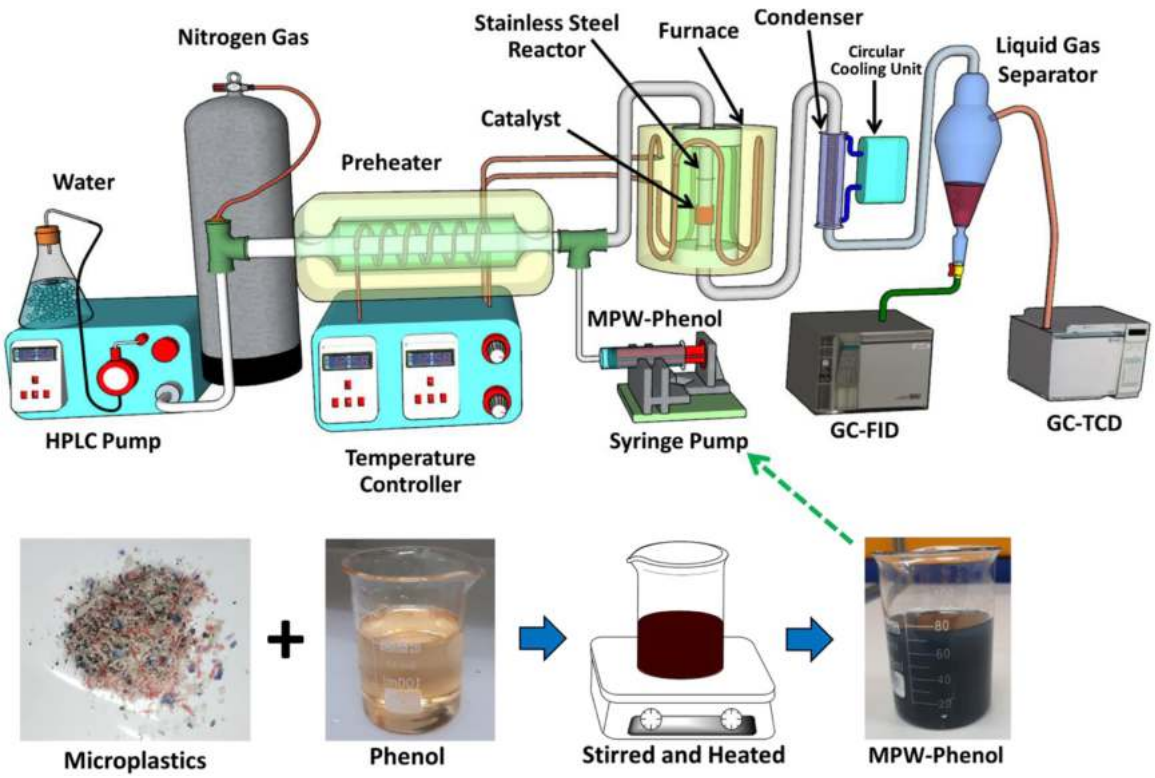

Fig. 1. A flow diagram of the pyrolysis-catalytic steam reforming of MPW-phenol reactor, adapted and reproduced from our previous work [3,6].

Ni and 2% Pt (named as 4Ni1Pt), 5% Ni and 5% Pt (named as 2Ni2Pt), 2% Ni and 8% Pt (named as 1Ni4Pt), and 10% Pt (named as Pt). All nanocatalysts were crushed, sieved to a size fraction between 35 and 34 mesh to obtain the particles sizes between 1.0 mm and 1.4 mm.

2.2. Characterization of the nanocatalysts

The dependence of S_{BET} of the calcined samples was measured by the FlowSorb III surface area analyzer instrument for S_{BET} measurement by dynamic single point method. 200–300 mg of each sample were first purified by degassing at 250 °C for 12 h using nitrogen flow before the BET test. X-ray diffraction (XRD) was carried out on a Bruker D8 Advance X-ray diffraction instrument (Cu Kα), the diffraction angle (2θ) from 5° to 100° was scanned. The crystalline phases were identified by JCPDS-ICDD (International Center for Diffraction Database) by X′Pert Highscore Plus software, and crystal size was calculated via the Scherrer equation. The compositions of the prepared samples were analyzed by an inductively coupled plasma (ICP) analyzer. Fourier transform infrared (FT–IR) spectra were measured by a Shimadzu IR-Prestige-21 model spectrometer with the KBr pellet method as a reference background to determine the functional groups present in the nanocatalysts and metal-support interactions. The samples for FT–IR measurements were mixed at a weight ratio of sample: KBr = 100:5, then ground and pressed by a pressure of 500 atm to a pellet with a diameter of 1.0 cm and a thickness of 0.3 mm. The infrared absorption spectra were recorded with the scanning range of 400–4000 cm^{-1}. The physicochemical properties such as reducibility, basicity, and acidity were analyzed using temperature-programmed reduction (H_2-TPR) and temperature-programmed desorption (CO_2-TPD & NH_3-TPD) analysis Micromeritics Chemisorb 2720 apparatus instrument. The same apparatus and the details of these analyses are reported in our previous research [4]. Field emission scanning electron microscopy (FESEM) images were obtained on FESEM, Zeiss, model Crossbeam 340 instrument to observe the nanocatalyst's surface morphology and the size distribution estimated using ImageJ software. Transmission electron microscope (TEM) and high-resolution transmission electron microscopy (HRTEM) micrographs were acquired with a JEOL JEM-ARM200F instrument at 200 kV. Thermogravimetric analyses (TGA) of carbon present on spent nanocatalysts were performed under dry airflow using Shimadzu TG-50 thermogravimetric apparatus. The carbon content, metal contents, functional groups, and BET surface area of used nanocatalysts were also analyzed by CHNS elemental analyzer, ICP test, FTIR spectra, and Micromeritics (FlowSorb III), respectively.

2.3. Catalyst screening

Microplastics formed from plastic trash such as bottles, bottle caps, plastic plates and cups, styrofoam objects, ropes, plastic bags, and straws were first gathered at Desaru beach in Johor, Malaysia. These garbage objects were cleaned, dried, and crushed using an industrial blender to make plastics with fewer than 5 mm^2 fragments. The wastes were then gently put into phenol and stirred for an hour at 80 °C with a volume ratio of 0.005:1. After that, the dark blue solution was transferred into an injection pump for the experiment. The reaction tests were carried out in a 6 mm i.d. fixed-bed continuous flow quartz reactor at standard atmospheric pressure and temperature from 500 °C to 700 °C, and a schematic flow diagram is shown in Fig. 1. Approximately 0.3 g of nanocatalyst diluted with 0.5 g of silicon carbide (benefits to rise catalytic performance [27,28]) was loaded inside the reactor; amid the catalyst bed, a K-type thermocouple was put to measure the temperature. Nanocatalysts were reduced at 600 °C before the reaction for an hour with a 35 mL/min flow of 10% H_2/Ar gas. The MPW-phenol solution was pumped with a syringe into the reactor, and nitrogen was used as a carrier gas and internal standard for gas analysis with 35 mL/min. MPW-phenol steam reforming was performed employing a water / MPW-phenol (0.04 mL/min) volume ratio of 9, and water was transfer by an HPLC pump into the reactor with 0.4 mL/min of flow rate. Water was vaporized via pre-heater at 200 °C before the reactor. After the reactor, a circular condenser was used to liquefy the condensable components analyzed by GC/MS (Agilent 7890B) and GC-FID (HP 5890

Table 1
Metal contents (ICP test), crystal size, BET surface area, pore-volume, and average pore diameter, basicity, reducibility, acidity, and data of the fresh nano-catalysts.

Catalysts	Ni (wt%)	Pt (wt%)	Crystal size (nm)	Surface area (m^2/g)	H_2-Consumption (mmol/g)	CO_2 uptake (mmol/g)	NH_3 uptake (mmol/g)
Ni	9.9	0	41.7	129.1	0.24	0.174	0.114
4Ni1Pt	8.04	2.03	33.5	104.8	2.16	3.41	0.196
2Ni2Pt	4.9	5.2	50.6	101.7	0.21	0	0
1Ni4Pt	2.1	7.98	80.4	98.6	0.3	0	0
Pt	0	10.1	78.4	89.2	0.07	0	0

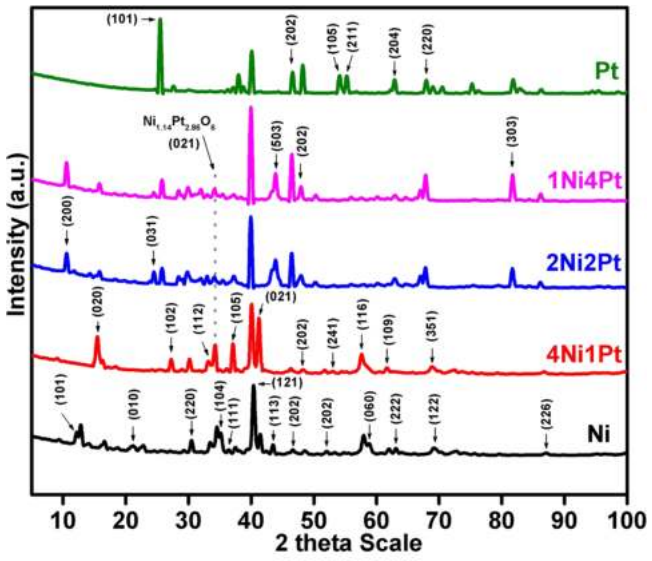

Figure 2 XRD curves of nano-catalysts

Fig. 2. XRD curves of nano-catalysts.

Table 2
The D-spacing (calculated via Bragg's equation) along with crystal size (calculated via Scherrer equation) for each XRD peak.

Peak position (2θ)	Theta (θ)	D-spacing (Å)	FWHM	Crystal Size, D (nm)
10.55	5.28	8.375	0.2086	38.2
12.14	6.07	7.282	0.3180	25.1
15.48	7.74	5.718	0.2068	38.8
24.49	12.23	3.631	0.3129	25.9
25.50	12.75	3.490	0.2086	39.0
27.36	13.68	3.258	0.0660	123.9
30.48	15.24	2.930	0.2086	39.5
33.24	16.62	2.693	0.3200	25.9
34.07	17.03	2.630	0.2608	31.9
35.25	17.63	2.544	0.2086	39.9
36.52	18.26	2.458	0.1565	53.5
37.11	18.55	2.421	0.2700	31.0
40.39	20.19	2.231	0.2608	32.5
41.51	20.75	2.174	0.2086	40.7
43.47	21.73	2.080	0.2888	29.6
43.89	21.95	2.061	0.3129	27.4
46.54	23.27	1.950	0.2608	33.2
48.29	24.15	1.883	0.2086	41.7
52.11	26.05	1.754	0.1043	84.8
53.81	26.90	1.702	0.1565	56.9
54.17	27.09	1.692	0.3129	28.5
55.29	27.64	1.660	0.3129	28.7
57.62	28.81	1.598	0.4200	21.6
61.70	30.85	1.502	0.5088	18.2
63.13	31.57	1.472	0.3180	29.3
67.95	33.98	1.378	0.2608	36.7
68.63	34.32	1.366	0.1908	50.4
69.28	34.64	1.355	0.8344	11.6
81.73	40.87	1.177	0.3129	33.6
87.09	43.54	1.118	0.4172	26.3

Series II). The non-condensed gas from the dried effluent stream was analyzed by GC-TCD (Agilent 6890 N). Eqs. (1) and (2) were used to determine the phenol conversion and yield of products in the pyrolysis-catalytic steam reforming of MPW-phenol processes in the fixed bed reactor employing various nanocatalysts.

$$Phenol \quad conversion \quad (\%) = \frac{[Phenol]_{in} - [Phenol]_{out}}{[Phenol]_{in}} \times 100 \tag{1}$$

$$Gas \quad yield \quad (\%) = \frac{moles \quad of \quad gas \quad obtained}{moles \quad of \quad gas \quad stoichiometric \quad potential} \times 100 \tag{2}$$

The flow rate of gaseous products (mL min^{-1}) was converted to (mmol min^{-1}) using a reference temperature of 25 °C at atmospheric pressure (1 mmol = 24.04 mL for volume conversion) [29].

3. Results

3.1. Catalyst characterization

The surface area and the metal loading of the calcined catalysts are shown in Table 1. The measured values obtained by the ICP analysis are all the metal loading values shown in Table 1. With the increment of Pt amount, the surface area decreases, most probably due to the surface coverage and plugging of the support pores by Pt particles.

The crystallinity and phases of as-prepared mono-metallic and bimetallic nanocatalysts were studied using the XRD technique. The average crystalline sizes measured utilizing the Scherrer equation are presented in Table 1, and the crystallite sizes varied from 33 to 80 nm for all nanocatalysts. The XRD curves of fresh nanocatalysts with different Ni to Pt ratios after the calcination step are shown in Fig. 2 and D-spacing (calculated via Bragg's equation) along with crystal size for each peak are listed in Table 2. The characteristic diffraction peaks of spinel phases at 2θ of 12.18° and 33.4° were observed can be assigned to characteristic peaks of (101) and (112) crystal phases and in agreement with the JCPDS number of 01–078–1510 for orthorhombic Ni_5TiO_7. All samples were almost the same in diffraction peaks at 2θ of 30.5° (220), 33.4° (012), 34.56° (100), 35.13° (104), 36.36° (111), 37.4° (105), 40.36° (121), 41.41° (021), 43.45° (113), 46.59° (202), 48.45° (202) and 87.03° (226). The cubic structure of $Ni_{2.44}Ti_{0.77}O_4$ was identified at 30.5° and in agreement with the JCPDS number of 01–084–0353. The diffraction peaks at 34.06° (021), 53.8° (241), and 68.63° (351) are matching to the orthorhombic phase structure of $Ni_{1.14}Pt_{2.86}O_6$ (JCPDS 01–076–1245), while orthorhombic phase structures of the TiO_2 detected at 36.36° and 40.36° peaks (JCPDS 01–082–1123) and 58.79° (060) and 69.05° (122) (JCPDS 01–082–1123). The rhombohedral phase structures of Al_2O_3 were noticed at 35.13° and 43.45° (JCPDS 00–001–1245) and 46.59° and 57.84° (116) (JCPDS 01–075–0785). The XRD peaks at 41.41° and 87.03° are ascribed to the rhombohedral phase structure of the Ni(TiO_3) (JCPDS 01–083–0209) whereas 21.1° (010) peak of rhombohedral Ni(TiO_3) in agreement with the JCPDS number of 01–077–0152. Various phase structures of Ti were observed at 37.4° (105) and 61.9° (109), which are corresponding to the hexagonal phase structures of Ti_3O (JCPDS 01–076–1644) while at 48.45° (202) and 63.06° (222) are in agreement with the monoclinic phase of TiO (JCPDS 01–075–0552). The peak at 51.91° (202) is assigned to the tetragonal phase structure of anatase TiO_2 and agrees with the JCPDS number of

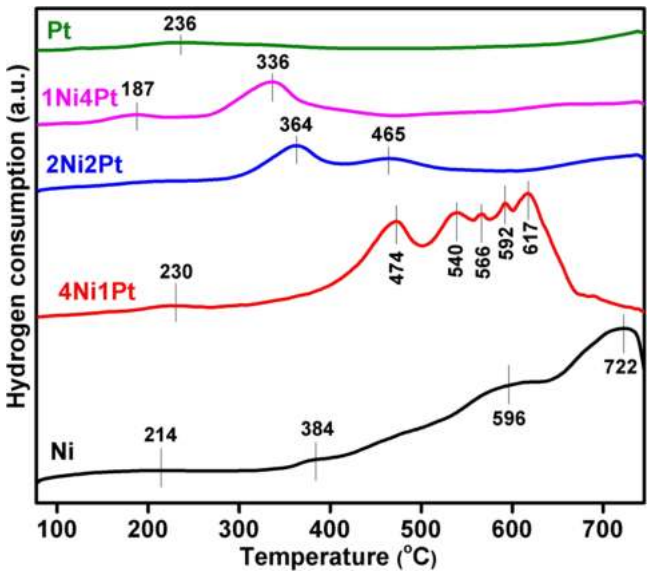

Fig. 3. Temperature programmed reduction (H_2-TPR) patterns of calcined nanocatalysts.

01–089–4203. The corresponding anatase TiO_2 peaks were also detected for the Pt, 2Ni2Pt and 1N4Pt samples at 25.49° (101), 54.04° (105), 55.22° (211), and 62.84° (204) and in agreement with JCPDS number of 01–084–1286. The characteristic peaks for Pt_8Ti ($2\theta = 81.8°$), marked by their indices (303) for these three nanocatalysts, revealed that they were in the tetragonal structure. The cubic structure of metallic Pt was seen for these three nanocatalysts at 67.87° (220) (JCPDS 00–001–1194). The relatively sharp XRD peaks specified a significant increase in the size of particles for bimetallic nanocatalysts. As seen in the 4Ni1Pt profile, two more diffraction peaks were observed at 16.58° (020) and 27.55° (102), which are ascribed as an orthorhombic phase of Al_3Pt_5 (JCPDS 03–065–1302) and hexagonal phase of Ti_6O (JCPDS 01–072–1807), respectively. The Al_3Pt_5 peak was detected for all three bimetallic samples (with crystal size of 33–80 nm) but in higher intensity for the 4Ni1Pt one. Thus, these bimetallic catalysts have regular profiles and, without splitting, consist of Al-Pt and Ni-Ti composites nano-powder. The orthorhombic phase structures of $AlPt_2$ were seen for the 2Ni2Pt and 1Ni4Pt samples at 10.8° (200) and in agreement with the JCPDS number 00–038–0740. The XRD patterns of these two samples showed peaks at 2θ of 24.43° and 43.91°, signifying the (031) and (503) crystal planes of the orthorhombic Al_6Pt phase, respectively. As seen for the bimetallic 4Ni1Pt diffraction curve, there is no evidence of Ni° or Pt° peaks suggesting the interactions of these metals with the Al_2O_3 and TiO_2 metal oxides.

The interaction between the TiO_2 and Al_2O_3 supports and the various Ni and Pt metals ratios are a key element in bimetallic nanocatalyst reducibility regulation. Although a strong metal-support interaction reduces metal reducibility, it could alter the electronic characteristics of metals or supports, change product selectivities, or improved nanocatalyst resistance to various kinds of deactivation. To examine the redox ability of the nanocatalysts, the H_2-TPR technique was conducted. The results were depicted in Fig. 3. The quantitative data of hydrogen consumption calculated based on the peak areas below the H_2-TPR curves are displayed in Table 1. The stoichiometry considered for Ni and Pt reduction $NiO_2 + 2\ H_2 \rightarrow Ni° + 2H_2O$ and $PtO_2 + 2H_2 \rightarrow Pt° + 2H_2O$. Catalysts with higher Pt content show signals at lower temperatures, and as the Pt metal loading was increased, the lower temperature peak dominated. For example, the signal at 236 °C, 187 °C, and 230 °C is attributed to the Pt oxide reduction, which suggests that most Pt species can be reduced to Pt° during the TPR experiment course confirms the PtO_x species interacting weakly with the Al_2O_3 support [30]. The lower reducibility properties for the catalysts with a higher platinum ratio may be because Pt increases the catalyst's average particle size, reducing the proportion of tiny particles with high concentrations of step and edge sites. Indeed, hydrogen can be stored at low temperatures within the crystalline lattice to form platinum hydride. As reduction peaks below 500 °C are ascribed to the reduction of Pt metals [31], the TPR peaks at 336 °C and 364 °C for 1Ni4Pt 2Ni2Pt catalysts, was attributed to the reduction of small Pt particles that were greatly spread on the support. These particles were found on the TiO_2 substrate as either solitary metallic particles or particles engaged in interactions with the support [32,33] or surface-capping oxygen [34,35]. These PtO-Al_2O_3 interactions are caused by the dissolution and incorporation of Al^{3+} ions in PtO crystallites which makes the disruption of the Pt-O bond difficult. Nevertheless, as the Ni metal loading was improved, the higher temperature peak dominated. H_2–TPR patterns of calcined Ni/Ti-Al exhibited a major reduction peak placed at about 722 °C, which was ascribed to NiO considerably interacting with the TiO_2 surface and might be due to the Ni^{2+} reduction in Ni/Ti-Al sample, while the peak centered at lower temperatures (214 and 384 °C) was the bulk NiO which are loosely bound with the support without any interaction with TiO_2 surface. The temperature peak at 596 °C could reduce moderately

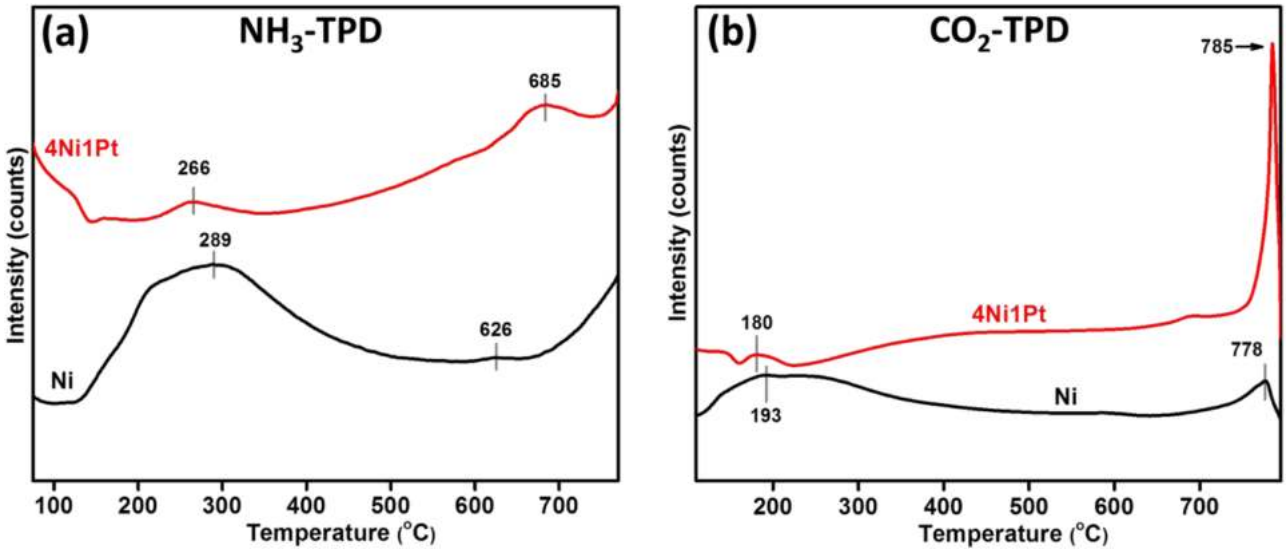

Fig. 4. (a) NH_3-TPD and (b) CO_2-TPD patterns of nanocatalysts.

reminded NiO and the support TiO_2 ($Ti^{4+} \rightarrow Ti^{3+}$). Ardiyanti et al. [36] stated that peak at 214 °C is signifying the reduction of Ni (III) oxide, at 384 °C ascribed the reduction of Ni(II) to Ni(0) species and the peaks at above 500 °C are linked to the reduction of surface Ni species strongly interact with the supports. At higher temperatures of 4Ni1Pt, the TPR profiles present complex reduction behavior. Indeed, the presence of reduction peaks at lower temperatures suggests that these catalysts have a greater redox potential than monometallic Ni catalysts. This might be because adding platinum to nickel catalysts causes hydrogen spillover, thus promoting the reduction of Ni^{2+} in the 4Ni1Pt nanocatalyst. The first peak, 230 °C is, corresponding to the simultaneous reduction of PtO_x species having weak interactions with alumina. In contrast, other peaks at higher temperatures are assigned for the reduction of NiO species having strong interaction with support. The H_2 chemisorption values given in Table 1 are consistent with higher hydrogen consumption for the bimetallic 4Ni1Pt nanocatalyst (2.16 mmol/g). Thus, it can be expected that the presence of Pt in low portion (4Ni1Pt) facilitated the reducibility behaviors of the bimetallic nanocatalysts which would promote the catalytic reforming and cracking reactions.

The surface acidity and basicity of a metal-supported catalyst are essential indicators of its activity and the probability of coke deposition during high-temperature exposure. Therefore, NH_3-TPD and CO_2-TPD were used to characterize the total acidity and basicity of the prepared nano-sized samples. The results are shown in Fig. 4, and quantitative data of NH_3 and CO_2 uptake calculated based on the peak areas below the TPD curves are displayed in Table 1. It can be anticipated that the acid and basic sites density slightly increased as the platinum is introduced to the nanocatalyst until 2 wt% (4Ni1Pt) and beyond which is reduced, and the acid-basic strength was negligible for the Pt, 1Ni4Pt, and 2Ni2Pt nanocatalysts (are not shown, because all TPD curves were flat lines without any CO_2 and NH_3 desorption peaks). Many acidic and basic sites are known to occur on supports, however, due to the relatively low metal concentration used in our nanocatalysts, most of the support surface is not occupied by metals. As a result, in the Pt-rich samples, certain Pt species may be directly positioned on the acid and basic sites in the support, reducing their quantity and cause to the acid-basic site's loss of the nanocatalysts. Another probability may be the existence of more surface hydroxyl groups attached to the support matrix in the bimetallic 1Ni4Pt and 2Ni2Pt and monometallic Pt nanocatalysts. The decrease of the acid sites on those three nanocatalysts can be involved with metal and support, and electron transfer electronic injection from Pt to support appears to be expected. NH_3-TPD of Pt and 4Ni1Pt nanocatalysts in Fig. 4(a) showed the first peaks at 289 °C and 266 °C, which specify the existence of medium acidic phases and related to ammonia adsorbed on ammonia cation, while those above 600 °C designate the attendance of strong acidic phases (Brønsted and Lewis acid). Ni–OH may act as a Brønsted acid site due to nickel's oxophilic character, while adjacent Pt could act as a Lewis acid site due to its electron deficit. Significantly, coordinatively unsaturated Pt and Ni atoms may adsorb ammonia molecules and absorb electrons, potentially creating additional Lewis acid sites throughout the synthesis.

Fig. 4(b) illustrates the CO_2-TPD analysis results of the nanocatalysts. The total basicities of the bimetallic 4Ni1Pt nanocatalyst, which has a more pronounced electron-donor characteristic, were higher than the monometallic Ni nanocatalyst. This high basicity boosts CO_2 adsorption capacity on the nanocatalyst surface and enhances the catalyst's resistance to carbon production by preventing the CO disproportionation process ($2CO \leftrightarrow C + CO_2$) [37]. It was commonly thought that the CO_2 desorption peaks at various temperatures might represent varying intensities of basic sites. The profiles showed that the monometallic Pt and bimetallic 4Ni1Pt possess weak (180 °C and 193 °C; OH^- groups) and strong (778 °C and 785 °C; isolated O^{2-} anions) basic sites. The density of total basic sites and the density of weak and strong basic sites grew exponentially for the bimetallic 4Ni1Pt based on the regions of CO_2 desorption peaks. It is suggested that 2 wt% Pt metal played a significant role in increasing the surface basicity strength; thus, the 4Ni1Pt catalyst

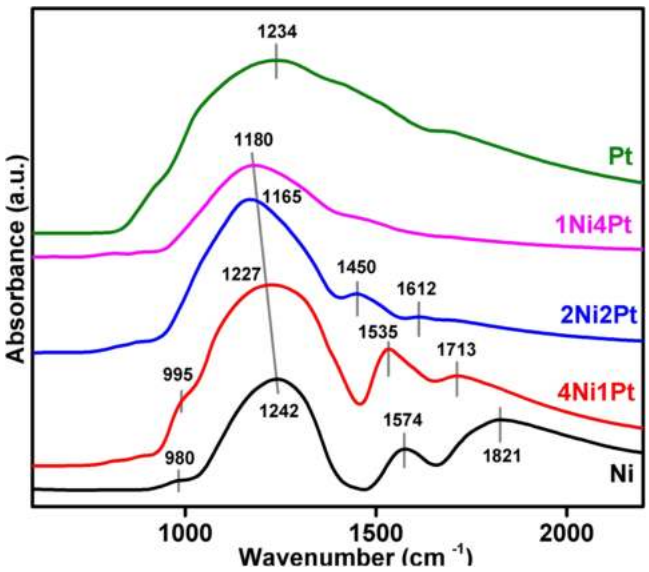

Fig. 5. The illustrative FTIR spectrum of the fresh nano-catalysts.

possessed the strongest basicity. Meanwhile, the desorption peak at high temperature, which corresponds to strong basicity, moves substantially higher. When the Lewis basicity of nanocatalysts was enhanced by 2 wt % of Pt, the capacity of nanocatalysts to chemisorb CO_2 was confirmed. Hence, the capability of CO_2 in preventing intermediate carbons produced from MPW-phenol steam reforming and cracking reactions will be improved due to its absorption ability. Thus, the TPD result implies that nanocatalysts' acidic and basic strength performs a vital role in explaining the catalytic performance for the pyrolysis-catalytic steam reforming reactions of MPW-phenol.

The FTIR spectra utilizing the KBr pellet method were conducted in the wavenumber range of 4000–400 cm^{-1} to inspect functional clusters present in the synthesized nanocatalysts, as shown in Fig. 5. The bands at the wavenumber 980 cm^{-1} and 1242 cm^{-1} are linked to C═C and C–O stretching vibrations for the monometallic Ni nanocatalyst. After employing 2 wi% of Pt, the small shoulder at the wavenumber of 995 cm^{-1} appeared, assigned to the C–O groups [38], and related to terminal NiO symmetric stretching was disappeared for the rest of the nanocatalysts. It's worth noting that XRD studies failed to identify this phase, most likely because it exists in the form of highly tiny crystallites that are widely distributed or in non-crystalline forms. The most intense band at 1242 shifted to 1227 cm^{-1} for the 4Ni1Pt bimetallic nanocatalyst, which is related to the C–N stretching modes and assigned to the formation of the formate and bicarbonate species presumably on the alumina support. This band shifted to a higher wavenumber (1180 and 1234 cm^{-1}) as the Pt content increase, which is probably related to metal-oxygen modes or OH out of plane deformations. The bands around 1574 cm^{-1} can be attributed to the asymmetrical extending mode of $\nu_{as}(COO^-)$ [39] and corresponding simultaneously to both Brønsted and Lewis acid sites [40]. The weak and broad bridge band at 1821 cm^{-1} is generally not observed on supported monometallic Pt and bimetallic 1Ni4Pt and 2Ni2Pt samples. They could be assigned to CO multi-bonded to NiTiAl alloy or at the interface between the metals and the surface, their frequencies being shallow. With the introduction of Pt, this band shifts slightly toward lower wavenumbers (1713 cm^{-1}), and it is in higher intensity for the 4Ni1Pt nanocatalyst than the other nanocatalysts, suggesting that 2 wt% Pt changes the surface support species and could indicate a large extent of Ni-Pt alloy formation.

To better understand the morphology of the calcined nanocatalyst and the average particle sizes, FESEM analysis was conducted, and the results are shown in Fig. 6. We chose the 4Ni1Pt sample for this characterization because of its better reducibility, acidity, and basicity

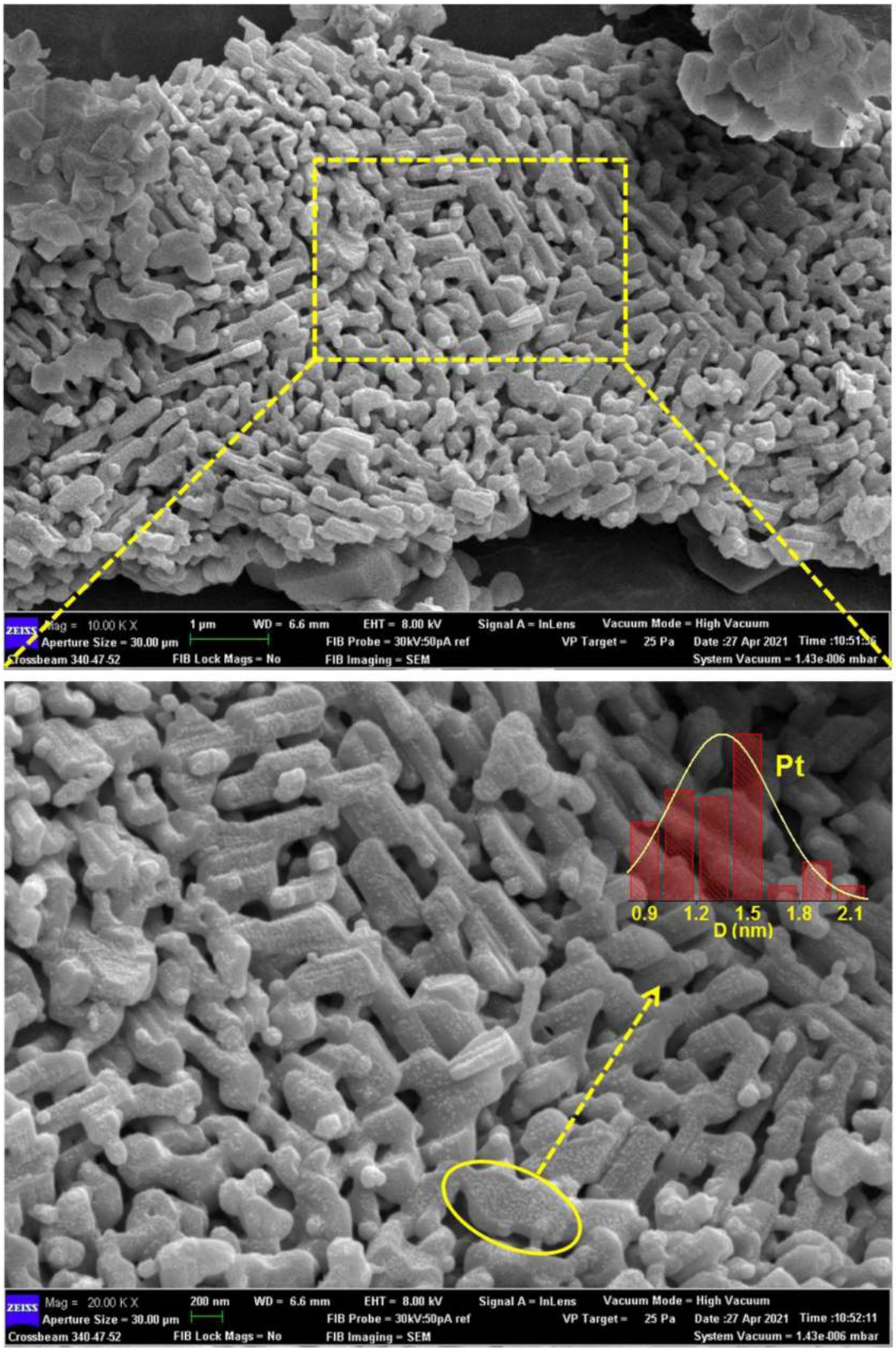

Fig. 6. FESEM images of the nano-catalyst along with corresponding size distribution histogram of TiO_2, Al_2O_3 Ni, and Pt components.

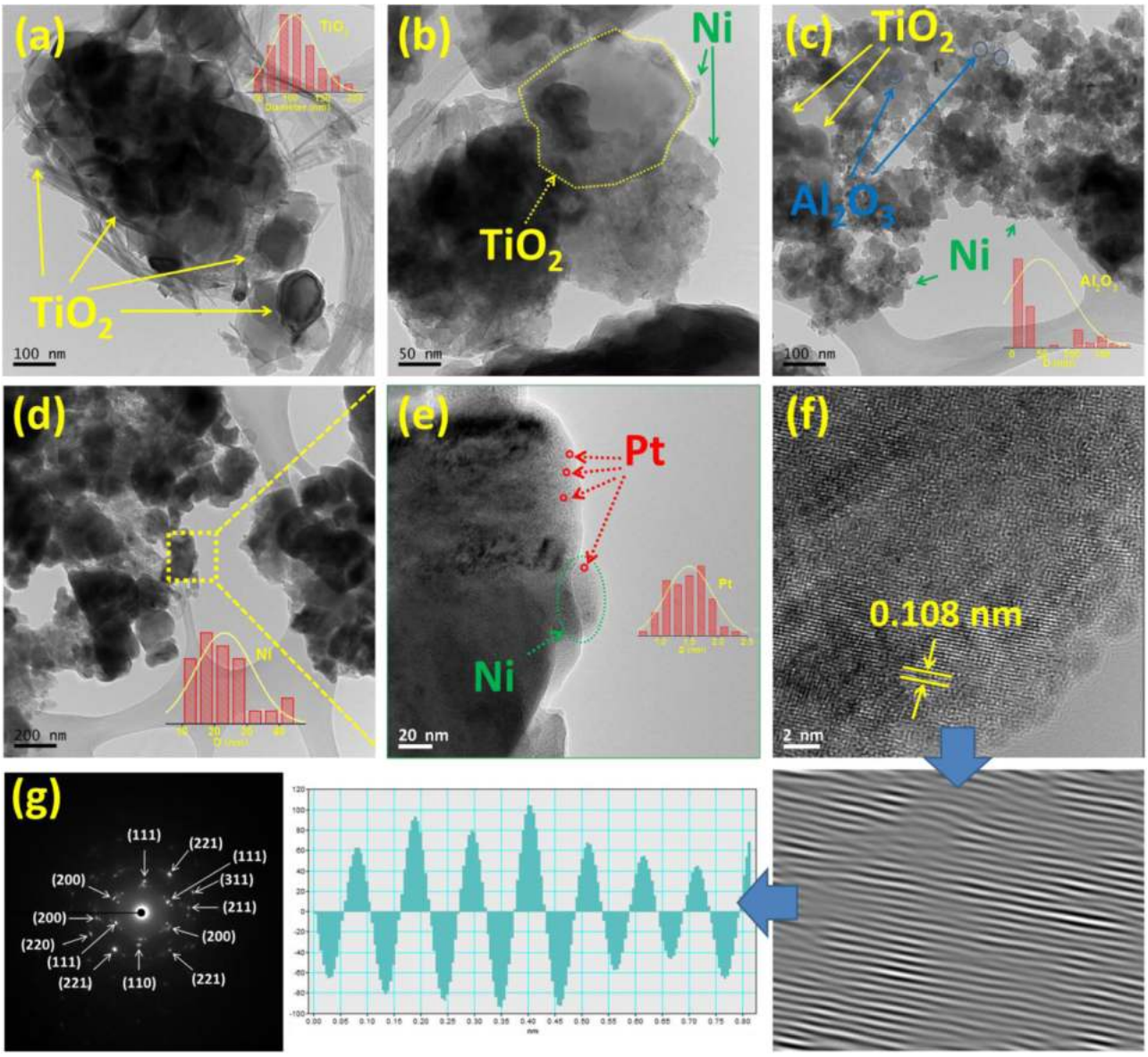

Fig. 7. TEM photos of (a) TiO_2, (b) Ni/TiO_2, (c) Ni/TiO_2-Al_2O_3, (d, e) $4Ni1Pt/TiO_2$-Al_2O_3, (f) HRTEM photos an (g) SAED images of $4Ni1Pt/TiO_2$-Al_2O_3 nanocatalyst.

properties than other nanocatalysts. Bimetallic nanocatalysts exhibit homogeneous Ni and Pt metals dispersion on the support surface and are spherically shaped and densely distributed, as shown by the analysis. These images also indicate that Pt metal has a smaller particles size (~1.3 nm) and more homogeneous morphology than Ni, but both prove their nanoscale sizes. The particle size of Al_2O_3 and TiO_2 are larger than

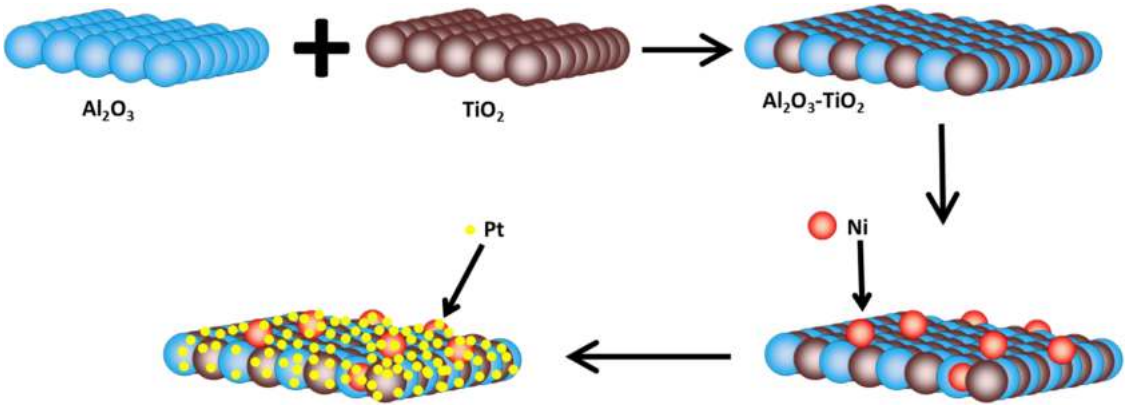

Fig. 8. Schematic illustration of the strategy for the $4Ni\text{-}1Pt/Al_2O_3$-TiO_2 bimetallic nanocatalyst.

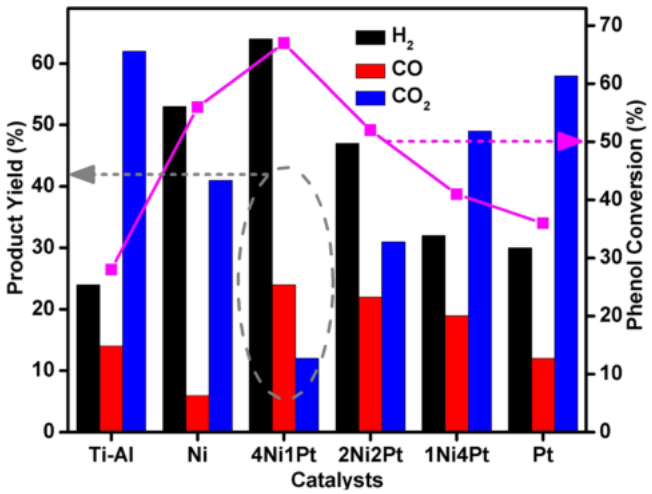

Fig. 9. Catalytic evaluation of different Ni to Pt ratio nanocatalysts and bare Ti-Al support in flow reactors. Reaction conditions: (catalyst: 0.3 g, pressure: 1 atm, reaction temperature: 500 °C, feed (MPW-phenol mixture) to water volume ratio of 1:9).

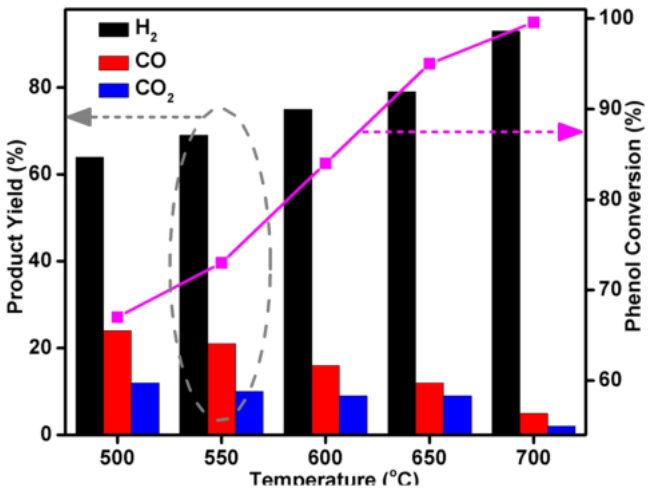

Fig. 10. Influence of reaction temperature on the phenol conversion and product yield. Reaction conditions: 4Ni1Pt catalyst: 0.3 g, pressure: 1 atm, feed (MPW-phenol mixture) to water volume ratio of 1:9.

those obtained in XRD analysis which might be ascribed to the fact that the crystal size determined from XRD data was related to the crystallized feature. Still, FESEM images disclosed the morphological structure of produced nanoparticle clusters. To get further insights into the morphology of the 4Ni1Pt nanocatalyst, TEM images of nano-catalyst are presented in Fig. 7, which approves their solid type similar to those with FESEM images. As seen in Fig. 7(d and e), smaller particles prevail on the supports surface, whereas big particles inside the porous support structure are found in larger quantities. However, the Pt particles are clearly more dispersed than Ni so that fewer Ni particles can be observed on the external surface of the support. It can be seen that Pt (~1.5 nm for 70 particles) and Ni (~22 nm for 27 particles) nanoparticles are dispersed on the supports with the lattice D-spacing of 0.108 nm. Pt atoms are distributed in the Ni particles and Al_2O_3-TiO_2 surface, which specifies that the particles have formed alloyed Ni-Pt nano-particles. The proposed schematic diagram for the dispersion of Ni and Pt nanoparticles on the Al_2O_3-TiO_2 surface is illustrated in Fig. 8. The SAED images in Fig. 7(g) show the polycrystals class of 4Ni-1Pt nanocatalyst in good agreement with the structure acquired in the X-ray diffraction curve.

3.2. Catalytic performance test

The use of different Ni to Pt ratios over Al_2O_3-TiO_2 supports the pyrolysis-catalytic steam reforming of MPW-phenol was examined in this section, and the results of phenol conversion and gaseous yield are displayed in Fig. 9. The major products in the gas stream in this reaction were H_2, CO, CO_2. In general, the 4Ni1Pt sample performed the best activity, and the order of the catalyst's performance, in terms of phenol conversion and hydrogen production, was found to be 4Ni1Pt > Ni> 2Ni2Pt > 1Ni4Pt > Pt > bare Al_2O_3-TiO_2 support. This observation is ideally in line with the calcined nanocatalysts' acidity, basicity, and reducibility behaviors. As seen, the monometallic Ni sample possesses a higher surface area than the bimetallic 4Ni1Pt nanocatalyst (see Table 1), but lewer catalytic activity, most probably due to coke deposition on its surface. As seen, higher 2 wt% of the amount of Pt metal displayed the lowest catalytic activity, probably due to the high sintering of the metallic phase and the lowest acidity, basicity, and redox capability of the catalysts. The increase in CO_2 and decrease in CO yields for higher Pt content catalysts can be ascribed to the cause of reverse water gas shift reaction ($CO + H_2O \leftrightarrow CO_2 + H_2$, $\Delta H^\circ = -41$ kJ/mol). The phenol conversion and hydrogen yield over

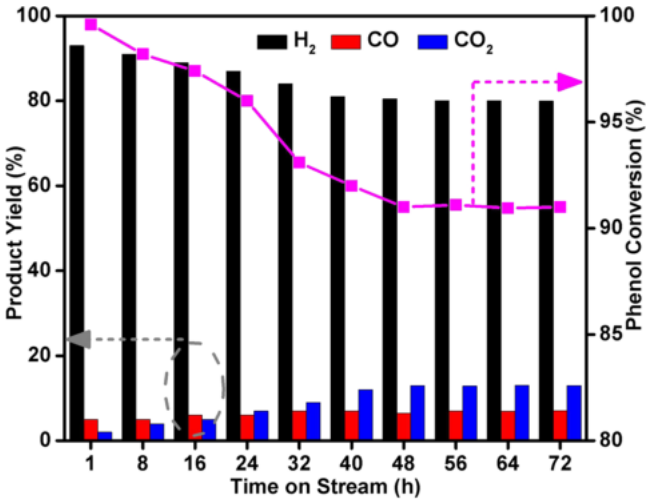

Fig. 11. Stability tests of 4Ni1Pt nanocatalyst at the temperature of 700 °C under the steam reforming conditions.

the 4Ni1Pt nanocatalyst were 67% and 64%, respectively. The higher acidic site of the bimetallic 4Ni1Pt nanocatalyst confirms that phenol decomposition has occurred during the reaction in which phenol decomposed to C_5H_6 + CO and its opposition with the O–H bond splitting and H-atom transfer reaction by H to produce the phenoxy radical (C_6H_5O). In phenol pyrolysis and combustion, this process is critical for regulating the H concentration [41]. Praveen et al. [42] stated that introducing a small amount of Cu metal in the $Cu_{0.1}$–$Mg_{0.2}/SiO_2$ catalyst had the maximum acidity and resulted in the highest 1,2-propanediol selectivity. According to the literature, increased surface acidity and a more significant number of strong acid sites may promote the cracking of large primary products of lignocellulosic feedstock breakdown into tiny molecules, enhancing the production of gaseous chemicals [43]. It is also known that using basic sites in catalysts promotes CO_2 adsorption and dissociation, which helps to gasify carbonaceous formations and reduces deactivation by coke production [44], and result in higher catalytic activity. In our previous research [45], we investigated the influence of the Ni to Co ratio on phenol conversion and hydrogen production. We found that higher Ni content such as Ni_3Co_1 catalyst exhibited the best catalytic performance amongst all the catalysts, signifying the existence of the main basic site and high coking resistance.

Table 3
Composition of liquid products after the reaction at 500 °C.

Compound	Formula	Ni	4Ni1Pt	2Ni2Pt	1Ni4Pt	Pt
Toluene	C_7H_8	0.1	0.1	0.2	0.2	0.2
Benzene, 1,3-dimethyl-	$C_{12}H_{16}$	0	0	0	0.1	0
Styrene	C_8H_8	0.2	0	0	0.3	0.3
Cyclooctatetraene	C_8H_8	0	0	0.1	0	0
Phenol	C_6H_6O	77.1	54.7	73.2	54.1	87.9
Benzoic acid, methyl ester	$C_8H_8O_2$	0	0	0	0	0.1
Naphthalene	$C_{10}H_8$	0.1	0	0	0	0
1,4-Benzenedicarboxylic acid, dimethyl ester	$C_{18}H_{26}O_6$	0.1	0.1	0	0	0.1
Dibenzofuran	$C_{12}H_8O$	0.1	0	0.1	0.2	0.2
N-Methyl-1-adamantaneacetamide	$C_{13}H_{21}NO$	0	0	0.1	0	0
Phthalic acid	$C_8H_6O_4$	0.2	0	0	0	0
Melamine, 3TMS derivative	$C_{12}H_{30}N_6Si_3$	0.1	0	0	0	0
Hexadecanoic acid, methyl ester	$C_{17}H_{34}O_2$	0.1	0	0	0	0
6-Methoxy-2-phenethyl-4H-chromen-4-one	$C_{18}H_{16}O_3$	0	0.1	0	0	0
9 H-Xanthene	$C_{13}H_{10}O$	0	0	0	0	0.1
3,4,5-Trimethoxy-.beta.-methyl-.beta.-nitrostyrene	$C_{12}H_{15}NO_5$	0.1	0	0	0	0
Pyrene	$C_{16}H_{10}$	0.1	0.1	0	0	0
Diisooctyl phthalate	$C_{24}H_{38}O_4$	0	0.1	0	0	0.1
Squalene	$C_{30}H_{50}$	0	1.5	0	0	0
1H,15H-Hexadecamethyloctasiloxane	$C_{16}H_{48}O_7Si_8$	0.3	1.6	0	0	0
1,2-Bis(trimethylsilyl)benzene	$C_{12}H_{22}Si_2$	0	16.5	0	0	0
Bis(trimethylsiloxy)methylsilane	$C_7H_{22}O_2Si_3$	0	1.9	0	0	0
Indole-2-one, 2,3-dihydro-N-hydroxy-4-methoxy-3,3-dimethyl-	$C_{11}H_{13}NO_3$	0	1.0	0	0	0
Silicic acid, diethyl bis(trimethylsilyl) ester	$C_3H_{12}O_4Si_2$	0	0	0	0	0.1
Cyclotrisiloxane, hexamethyl-	$C_6H_{18}O_3Si_3$	3.1	0	12.9	26.1	2
Tetrasiloxane, decamethyl-	$C_{10}H_{30}O_3Si_4$	16.6	1.2	8.2	0	0
4-tert-Amylphenol, TMS derivative	$C_{11}H_{16}O$	0	1.2	0	0	0
Cyclohexane-1,3-dione, 2-allylaminomethylene-5,5-dimethyl-	$C_{12}H_{17}NO_2$	0	14	0	0	0
Bis(2-ethylhexyl) phthalate	$C_{24}H_{38}O_4$	0	3.7	0	0.4	0
Tris(tert-butyldimethylsilyloxy)arsane	$C_{18}H_{45}AsO_3Si_3$	1.4	2.2	2.8	5.2	1.1
4-(4-Hydroxyphenyl)-4-methyl-2-pentanone, TMS derivative	$C_{12}H_{16}O_2$	0	0	1.1	8.9	0
Benzo[h]quinoline, 2,4-dimethyl-	$C_{15}H_{13}N$	0	0	0	2.3	0.8
1,2-Benzisothiazol-3-amine, TBDMS derivative	$C_{13}H_{20}N_2SSi$	0	0	0	0.5	0
Methyltris(trimethylsiloxy)silane	$C_{10}H_{30}O_3Si_4$	0.3	0	0	1.7	7
2,4,6-Cycloheptatrien-1-one, 3,5-bis-trimethylsilyl-	$C_{13}H_{22}OSi_2$	0	0	0.3	0	0
1,2,4-Benzenetricarboxylic acid, 4-dodecyl dimethyl ester	$C_{23}H_{34}O_6$	0	0	1.0	0	0
SUM		100	100	100	100	100

The 4Ni1Pt nanocatalyst showed higher redox properties (see Table 1 and Fig. 3) and strong Pt-Al and Ni-Ti interactions (see Fig. 2) as confirmed by H_2-TPR and XRD analysis, respectively. This reducibility and strong metal-support interactions create more active sites for the reaction and result in higher catalytic performance. It also could be suggested that the synergistic influence of Ni–Pt alloy (as confirmed by TEM analysis, Fig. 7e) acts an important part; that is, Pt is better at adsorbing hydroxyl radicals from water molecules, whereas Ni has a strong activation capacity for C–C and C–H bonds. The FTIR result (Fig. 5) illustrated that the 4Ni1Pt sample posses a C–O bond at 995 cm^{-1}. This bond is back bonding in which reactant molecules donate electrons to the metal and metal donate electrons to the molecule, a vital bond component in the reaction. Combining with such chemical and physical properties of 4Ni1Pt nanocatalyst, we believe the enhancement in the stability is expected; thus, we conducted the impact of temperature and time on stream tests as seen in Fig. 10 and Fig. 11.

The temperature has essential impacts on the activity of the bifunctional 4Ni1Pt nanocatalyst for hydrogen generation from pyrolysis-catalytic steam reactions of MPW-phenol. The conversion of phenol and the distribution of products for the pyrolysis-catalytic steam reforming reactions over the 4Ni1Pt nanocatalyst is presented in Fig. 10. The C–C bond scission and water gas shift reaction are regulating the reforming product. The water-gas shift reaction, which takes CO molecules in the presence of steam during the reforming process, plays a significant role in hydrogen generation. Metals, in contrast, regulate the activation of C–C and C–H bonds, and basic sites of the support are responsible for transferring –H and –OH hydroxyl [2]. Both hydrogen yield and phenol conversion were increased with temperature from 64% and 67% at 500 °C to 93% and 99.6% at 700 °C, respectively. This improvement in catalytic activity with the temperature is because phenol steam reforming ($C_6H_5OH + 5\ H_2O \rightarrow 6CO + 8\ H_2$, $\Delta H^\circ = 710.91$ kJ/mol) is highly endothermic. Published studies have obtained the same result of improving phenol conversion with temperature [46–48]. Gabriella et al. [49] used 5 wt% Ni/Al_2O_3 catalysts for hydrogen generation from ethanol–phenol steam reforming. They achieved 85% of hydrogen yield and 100% of phenol conversion at 700 °C, but that catalyst can be active only at the range of 600–750 °C in the time scale. As seen in the result, CO and CO_2 yields showed the opposite trend of hydrogen production and phenol conversion. They were significantly decreased from 24% and 12% at 500 °C to 5% and 2% at 700 °C, with increasing CO and CO_2 yields confirming the existence of water gas shift reaction ($CO + H_2O \leftrightarrow CO_2 + H_2$). This signified that the water gas shift reaction is crucial for achieving the high percentage of phenol conversion and hydrogen yield. Khaled et al. [50] employed 10% Ni/TiO_2-B for hydrogen generation from phenol steam reforming reaction. They found that 93.7% of phenol conversion and 71.2% of hydrogen yield were achieved at 700 °C. Tariq et al. [51] also used 10% NiO-5% Co_3O_4 NCs/TiO_2 catalysts and reached 69.91% of hydrogen yield 78.4% of phenol conversion at 700 °C. The previous work's findings regarding hydrogen yield and phenol conversion were slightly less than the current work achievements. In the phenol steam reforming reaction, the nanocatalyst synthesis technique, metal loading, reaction condition, and promoter employed are all factors that affect the activity, selectivity, and stability of nanocatalysts.

The performance and stability of 4Ni1Pt nanocatalyst studied under pyrolysis-catalytic steam reforming conditions were also evaluated in terms of product yield, phenol conversion, and stability at 700 °C for three days of time-on-stream. There were no vast differences observed, especially after 40 h of time-on-stream. Phenol conversion decreased from 99.6% to 92% and remained almost lined up for the rest of the

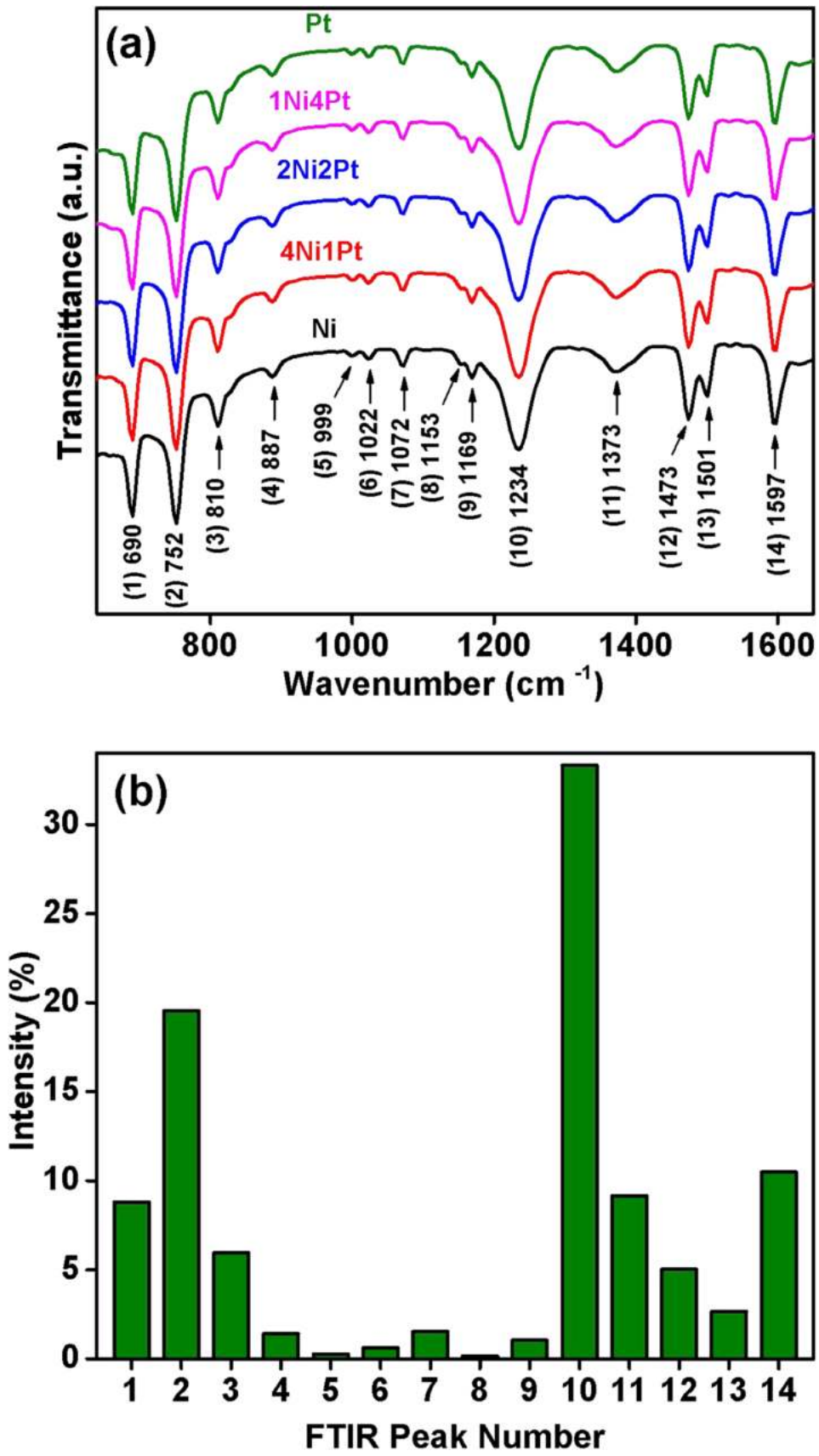

Fig. 12. (a) FTIR spectra of total pyrolysis products after the reaction at 500 °C and (b) summary of bands FTIR intensities.

reaction time. Besides, hydrogen yield decreased from 93% to 81% after a two-day reaction and became stable afterward. According to the above discussion, the bifunctional 4Ni1Pt nanocatalyst has good physical and chemical properties, resulting in long-term stability.

3.3. Liquid products composition

Only a small fraction of the chemical identities in liquid fuels can be captured by GC–MS. In GC–MS, small and high molecular weight molecules exhibit the same behavior. The fuel's composition was then calculated by dividing the quantity of each analyte by the total number of products identified. The GC–MS analysis may be used to evaluate the pyrolysis products produced, and the chemical compositions are shown in Table 3; all the detected components have been listed. Many scientists clustered the discovered important liquid components into a few clusters: naphthalenes, aromatics, and aliphatics to simplify the GC-MS findings [52–54]. The acidic catalysts result in shorter chain hydrocarbons because of their high cracking capability [55]. However, since the cracking process occurs primarily on the catalysts' outer surface, the less acidic catalysts promote the synthesis of long-chain hydrocarbons [56]. More phenol was converted into the liquid product for the bimetallic 4Ni-1Pt and 1Ni-4Pt nano-catalysts than other samples. GC-MS data of liquid product shows that most of the chemical components for monometallic Ni sample were aliphatic (16.6% of $C_{10}H_{30}O_3Si_4$) and then aromatic (3.1% of $C_6H_{18}O_3Si_3$). A high percentage of aromatic $C_6H_{18}O_3Si_3$ was also observed for the 2Ni2Pt (12.9%), 1Ni4Pt (26.1%), and Pt (2%) samples too. Generally, the strong existence of these components in great amounts implies that the produced substances from the pyrolysis process were predictably value-added products. With imploying 2 wt% of Pt, new aromatics (47.2%) such as 1,2-Bis(trimethylsilyl)benzene ($C_{12}H_{22}Si_2$, 16.5%), $C_{11}H_{13}NO_3$ (1%), $C_{11}H_{16}O$ (1.2%), $C_{12}H_{17}NO_2$ (14%), $C_{24}H_{38}O_4$ (3.7%), as well as 6.8% aliphatics such as Squalene ($C_{30}H_{50}$, 1.5%), $C_7H_{22}O_2Si_3$ (1.9%), $C_{10}H_{30}O_3Si_4$ (1.2), $C_{18}H_{45}AsO_3Si_3$ (2.2%) were observed. Mihai et al. [57] indicated that the liquid products with the side chain might be removed after employing a cracking reaction at higher temperatures. Results show that small traces of toluene (C_7H_8), benzene ($C_{12}H_{16}$), styrene (C_8H_8), and cyclooctatetraene (C_8H_8) were detected in the liquid products. Secondary products constituents enter the pores of the nanocatalysts, forming tiny hydrocarbons. Cyclization and aromatization within the nanocatalyst pores also generate the aromatic group [58,59]. The observed toluene and styrene, even in low portion, also specify that styrene in this research possibly rises mostly from the natural molecules pyrolysis. Overall, the abundance of compounds combining hydrogen and carbon in the findings above indicates that the liquid products generated have the potential to be utilized as combustible fuel sources. The produce liquid products also have numerous specific possible applications, such as air fresheners, laundry products, cleaners, generation of fungicide Propiconazole, thiophene, stabilizers, pharmaceuticals, etc.

The FTIR analysis was conducted to get further insight into the functional groups in the produced liquid products after pyrolysis reaction, and results with peaks intensities are depicted in Fig. 12. These functional groups benefit from distinguishing specific chemical compounds, like alkanes, olefins, benzene, alcohols, etc. It may also be used to determine pyrolysis products' types and learn more about how pyrolysis works. Also, the results from FT-IR analysis were found to agree with the GC-MS results, and the main products could be phenolic compounds. The FTIR spectra show one pronounced absorbance peak of C–H out of plane bending was observed for the aromatic hydrocarbons with high intensities at 690 cm^{-1}, 752 cm^{-1}, 810 $cm^{-1,}$ and 887 cm^{-1}. Peaks at 999 cm^{-1} and 1022 cm^{-1} C–O(H) stretching vibrations of phenols and ethers while wavenumber of 1072 cm^{-1} is ascribed to the C–O(H) stretching vibrations acetic acid. Specifically, 1153 cm^{-1} and 1169 cm^{-1} peaks confirm the presence of the C–O functional groups, while the prominent transmittance peak at 1234 cm^{-1} in FTIR spectra was a typical stretching vibration peak of the C–O(H) groups. The bands

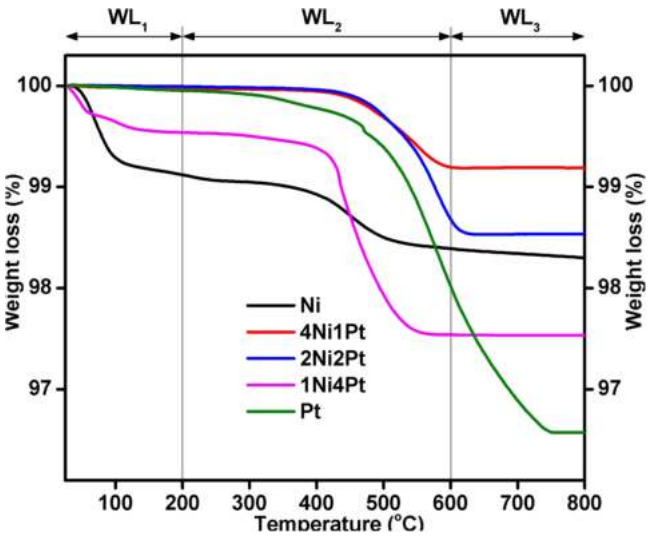

Fig. 13. Thermogravimetric curves of catalysts after pyrolysis-catalytic steam reforming at 500 °C.

at 1473 cm^{-1}, 1501 cm^{-1}, and 1597 cm^{-1} represent the existence of C═C–C aromatic stretch contributing toward the more aromatic compounds in the product. From the FTIR curve, it was easy to find that some intensities of transmittance peaks are high, and some are low. Chain breaking occurred arbitrarily in any region of the polymer due to the low degree of branching and high intermolecular force of microplastics molecules, implying that microplastics pyrolysis is an irregular chain scission process. As a result, all peaks in the FTIR spectra obtained in this research do not indisputably match the peaks of a single substance. Regardless, certain peaks may belong to several compounds simultaneously, covering the existence of weaker peaks.

3.4. Characterizations of used catalysts

Analysis of spent catalysts to have further insight into the coke deposition on the catalyst with valuable metals such as platinum and nickel used in this study strongly impacts stability and reusability. The deposited coke can cover the active center and subsequently result in the catalysts' deactivations. In this respect, the characterization of the used catalyst after reaction at 500 °C through TGA, ICP, CHNS, and BET surface area contributes to considerate their deactivation by coke formation. Fig. 13 and Table 4 show the results of TGA analysis on spent catalysts to estimate the quantity of coke produced during the process. The percentage of total coke deposition decreases in the following order: Pt (3.42%) > 1Ni4Pt (2.47%) > Ni (1.7%) > 2Ni2Pt (1.46%) > 4Ni1Pt (0.82%). This result is consistent with pyrolysis-catalytic steam reforming reactions of MPW-phenol results, as shown in Fig. 9. This also follows the tendency of the percentage of carbon content and defense in BET surface area and ICP test. The weight loss in the sample because of the coke gasification is shown by the sample weight behavior, which reveals various kinds of carbonaceous species produced on the catalysts. All the catalysts depicted three different stages in their thermal decomposition behaviors. The first weight loss took place below 200 °C (WL_1), conforming to the removal of water molecules. As seen in the TGA curves, the monometallic Ni and bimetallic 1Ni4Pt nanocatalysts had the 0.88% and 0.46% of sudden weight losses in the WL_1 region, probably because of the presence of amorphous carbon species and thermal desorption of water molecules. TGA of the spent catalysts shows dramatic weight losses in the region of 200–600 °C (WL2) corresponding to the oxidation of coke deposits with low stabilities. The TGA curve illustrated that only the monometallic Pt sample had the highest weight loss in 600–800 oC (WL3), associated with the burning of highly stable coke deposits. The coke oxidation at high temperature confirms the coke

Table 4
Weight loss, carbon and metal (ICP test) contents, and surface area of the used catalysts.

Catalysts	Weight loss (%)			Total weight loss (%)	Ni (wt %)	Pt (wt %)	Carbon Content (wt%)	Fresh catalyst Surface area (m^2/g)[a]	Spent catalyst Surface area (m2/g)[b]	Difference between surface area (a-b)
	WL_1	WL_2	WL_3							
Ni	0.88	0.73	0.09	1.7	7.1	0	11.5	129.1	100.4	28.7
4Ni1Pt	0.02	0.78	0.02	0.82	7.9	1.8	0.06	104.8	102.6	2.2
2Ni2Pt	0.01	1.3	0.15	1.46	3.8	4.9	9.3	101.7	91.9	9.8
1Ni4Pt	0.46	2	0.01	2.47	1.5	4.7	14.2	98.6	69.3	29.3
Pt	0.05	1.93	1.44	3.42	0	6.2	28.7	89.2	52.8	36.4

deposited on the Pt sample is typically filamentous or graphitic in nature [60]. The reactivity of graphitic-like carbon with oxygen or steam, according to former studies, is lower than amorphous type carbons [61, 62]. Alternatively, the spent 4Ni1Pt nanocatalyst does not show a significant weight loss (< 1%) after pyrolysis-catalytic steam reforming reactions of MPW-phenol, suggesting the lack of coke on it.

4. Conclusion

In summary, different ratios of Ni to Pt nanocatalysts supported on Ti-Al were utilized for pyrolysis-catalytic steam reforming conditions of microplastics wastes liquefied in phenol to generate hydrogen and valuable liquid fuel. The physical and chemical characterization of the synthesized catalysts via the hydrothermal method was found to be in nano-sized particles. The employing 2 wt% of Pt metal (4Ni1Pt) significantly increased the acidity with both Brønsted and Lewis acid, reducibility with strong metal support interactions, basicity with Lewis basic sites, and catalytic activity and stability. The strong metal-support interaction, reducibility, basicity and acidity properties of the prepared nano-sized samples seem to play a crucial role more than the surface area. The maximum phenol conversion and hydrogen yield were found to be 67% and 64% at 500 °C, respectively. In comparison, an almost full amount of phenol component (99.6%) was converted at 700 °C for the bifunctional 4Ni1Pt nanocatalyst. Liquid fuels that produced after the reaction were consisted of numerous valuable components such as: $C_{12}H_{22}Si_2$ (1,2-bis(trimethylsilyl)benzene), $C_6H_{18}O_3Si_3$ (cyclotrisiloxane, hexamethyl-), $C_{10}H_{30}O_3Si_4$ (tetrasiloxane, decamethyl-), $C_{12}H_{17}NO_2$ (cyclohexane-1,3-dione, 2-allylaminomethylene-5,5-dimethyl-), $C_{24}H_{38}O_4$ (bis(2-ethylhexyl) phthalate), $C_{18}H_{45}AsO_3Si_3$ (tris(tert-butyldimethylsilyloxy)arsane), $C_{12}H_{16}O_2$ (4-(4-Hydroxyphenyl)− 4-methyl-2-pentanone, TMS derivative), and etc. The results of this study afford experimental groundwork for the recovery of microplastic waste and the development of bifunctional nanocatalyst utilized for hydrogen and useful liquid fuels generation from waste substances. The situation and circumstances must be completely understood to discover industrial ways to solve and utilize the microplastics that existed in oceans and soil, underlining the need for further investigations in this area of research.

Declaration of Competing Interest

The authors declare that they have no known competing financial interests or personal relationships that could have appeared to influence the work reported in this paper.

Acknowledgment

The primary author, Walid Nabgan, is thankful for the support from Universiti Teknologi Malaysia in the form of the Post-Doctoral Fellowship Scheme "Simultaneous heavy metals ions and organic pollutants photoredox reactions over SiO_2/ZrO_2 based catalysts under solar-light irradiation" (PDRU Grant number: 05E49). In addition, the authors acknowledge the financial support given for this work by Universiti Teknologi Malaysia (UTM) under the Collaborative Research Grant (CRG) number 07G61, 07G59, and 07G62.

References

[1] A. Rahman, A. Sarkar, O.P. Yadav, G. Achari, J. Slobodnik, Sci. Total Environ. 757 (2021), 143872.
[2] W. Nabgan, B. Nabgan, T.A. Tuan Abdullah, A.A. Jalil, A. Ul-Hamid, M. Ikram, A. H. Nordin, A. Coelho, J. Anal. Appl. Pyrolysis 154 (2021), 105018.
[3] W. Nabgan, B. Nabgan, T.A. Tuan Abdullah, H. Alqaraghuli, N. Ngadi, A.A. Jalil, B. M. Othman, A.M. Ibrahim, T.J. Siang, Int. J. Hydrog. Energy 45 (2020) 22817.
[4] W. Nabgan, B. Nabgan, T.A. Tuan Abdullah, N. Ngadi, A.A. Jalil, N.S. Hassan, S. M. Izan, W.S. Luing, S.N. Abdullah, F.S.A. Majeed, Int. J. Hydrog. Energy 45 (2020) 6302.
[5] W. Raza, J. Lee, N. Raza, Y. Luo, K.-H. Kim, J. Yang, J. Ind. Eng. Chem. 71 (2019) 1.
[6] W. Nabgan, B. Nabgan, T.A. Tuan Abdullah, N. Ngadi, A.A. Jalil, N.A.A. Fatah, H. Alqaraghuli, M. Tahir, J. Anal. Appl. Pyrolysis 150 (2020), 104860.
[7] W. Nabgan, B. Nabgan, T.A.T. Abdullah, N. Ngadi, A.A. Jalil, A.H. Nordin, N.A. F. Abd Latif, N.F.H. Othman, Catal. Sustain. Energy 7 (2020) 45.
[8] W. Mulewa, M. Tahir, N.A.S. Amin, Chem. Eng. J. 326 (2017) 956.
[9] K.S. Baamran, M. Tahir, J. Clean. Prod. 311 (2021), 127519.
[10] D.J.M. de Vlieger, A.G. Chakinala, L. Lefferts, S.R.A. Kersten, K. Seshan, D.W. F. Brilman, Appl. Catal. B: Environ. 111–112 (2012) 536.
[11] A. Yamaguchi, N. Hiyoshi, O. Sato, M. Osada, M. Shirai, Chem. Lett. 39 (2010) 1251.
[12] L. Zhang, P. Champagne, C. Xu, Bioresour. Technol. 102 (2011) 8279.
[13] M.S.H.K. Tushar, A. Dutta, C. Xu, Appl. Catal. B: Environ. 189 (2016) 119.
[14] C. He, J. Zheng, K. Wang, H. Lin, J.-Y. Wang, Y. Yang, Appl. Catal. B: Environ. 162 (2015) 401.
[15] Z. Xie, B. Yan, J.H. Lee, Q. Wu, X. Li, B. Zhao, D. Su, L. Zhang, J.G. Chen, Appl. Catal. B: Environ. 245 (2019) 376.
[16] G. Li, J. Han, H. Wang, X. Zhu, Q. Ge, ACS Catal. 5 (2015) 2009.
[17] J. Niu, Y. Wang, S.E. Liland, S.K. Regli, J. Yang, K.R. Rout, J. Luo, M. Rønning, J. Ran, D. Chen, ACS Catal. 11 (2021) 2398.
[18] A.G. Chakinala, W.P.M. van Swaaij, S.R.A. Kersten, D. de Vlieger, K. Seshan, D.W. F. Brilman, Ind. Eng. Chem. Res. 52 (2013) 5302.
[19] M. García-Diéguez, I.S. Pieta, M.C. Herrera, M.A. Larrubia, L.J. Alemany, J. Catal. 270 (2010) 136.
[20] M. García-Diéguez, I.S. Pieta, M.C. Herrera, M.A. Larrubia, L.J. Alemany, Appl. Catal. A: Gen. 377 (2010) 191.
[21] T. Abbas, M. Tahir, N.A. Saidina Amin, Ind. Eng. Chem. Res. 58 (2019) 517.
[22] K.S. Baamran, M. Tahir, B. Tahir, H. Alias, M.A.C. Yunus, Chem. Eng. 83 (2021).
[23] E.T. Kho, J. Scott, R. Amal, Chem. Eng. Sci. 140 (2016) 161.
[24] X. Gao, S.R. Bare, J.L.G. Fierro, M.A. Banares, I.E. Wachs, J. Phys. Chem. B 102 (1998) 5653.
[25] A.L. Alberton, M.M.V.M. Souza, M. Schmal, Catal. Today 123 (2007) 257.
[26] A. Sadeq Al-Fatesh, S. Olajide Kasim, A. Aidid Ibrahim, A. Hamza Fakeeha, A. Elhag Abasaeed, R. Alrasheed, R. Ashamari, A. Bagabas, Catalysts 9 (2019) 188.
[27] W. Nabgan, T.A. Tuan Abdullah, R. Mat, B. Nabgan, U.A. Asli, A. Johari, J. Teknol. 78 (2016) 77.
[28] T.A.T. Abdullah, W. Nabgan, M.J. Kamaruddin, R. Mat, A. Johari, A. Ahmad, Appl. Mech. Mater. 493 (2014) 39.
[29] D.B. Nguyen, W.G. Lee, J. Ind. Eng. Chem. 32 (2015) 187.
[30] T. Deng, H. Liu, Green. Chem. 15 (2013) 116.
[31] S.A. Singh, G. Madras, Appl. Catal. A: Gen. 518 (2016) 102.
[32] S. Subramanian, J.A. Schwarz, Appl. Catal. 74 (1991) 65.
[33] A. Djeddi, I. Fechete, F. Garin, Top. Catal. 55 (2012) 700.
[34] C. Zhang, H. He, K.-i Tanaka, Appl. Catal. B: Environ. 65 (2006) 37.
[35] W.S. Epling, P.K. Cheekatamarla, A.M. Lane, Chem. Eng. J. 93 (2003) 61.
[36] A.R. Ardiyanti, S.A. Khromova, R.H. Venderbosch, V.A. Yakovlev, H.J. Heeres, Appl. Catal. B: Environ. 117–118 (2012) 105.
[37] F. Meshkani, M. Rezaei, Int. J. Hydrog. Energy 35 (2010) 10295.
[38] Z. Zhang, Y. Wang, K. Sun, Y. Shao, L. Zhang, S. Zhang, X. Zhang, Q. Liu, Z. Chen, X. Hu, J. Energy Chem. 43 (2020) 208.
[39] K.I. Hadjiivanov, D.A. Panayotov, M.Y. Mihaylov, E.Z. Ivanova, K.K. Chakarova, S. M. Andonova, N.L. Drenchev, Chem. Rev. 121 (2021) 1286.
[40] Q. Sun, Y. Fu, J. Liu, A. Auroux, J. Shen, Appl. Catal. A: Gen. 334 (2008) 26.
[41] L. Pratali Maffei, M. Pelucchi, T. Faravelli, C. Cavallotti, React. Chem. Eng. 5 (2020) 452.
[42] P. Kumar, A.K. Shah, J.-H. Lee, Y.H. Park, U.L. Štangar, Ind. Eng. Chem. Res. 59 (2020) 6506.
[43] A. Sharma, V. Pareek, D. Zhang, Renew. Sustain. Energy Rev. 50 (2015) 1081.
[44] V. García, J.J. Fernández, W. Ruíz, F. Mondragón, A. Moreno, Catal. Commun. 11 (2009) 240.

[45] W. Nabgan, T.A. Tuan Abdullah, R. Mat, B. Nabgan, Y. Gambo, S. Triwahyono, Int. J. Hydrog. Energy 41 (2016) 22922.
[46] K. Polychronopoulou, A. Bakandritsos, V. Tzitzios, J.L.G. Fierro, A.M. Efstathiou, J. Catal. 241 (2006) 132.
[47] D.A. Constantinou, J.L.G. Fierro, A.M. Efstathiou, Appl. Catal. B: Environ. 95 (2010) 255.
[48] W. Nabgan, T.A. Tuan Abdullah, R. Mat, B. Nabgan, S. Triwahyono, A. Ripin, Appl. Catal. A: Gen. 527 (2016) 161.
[49] G. Garbarino, E. Finocchio, A. Lagazzo, I. Valsamakis, P. Riani, V.S. Escribano, G. Busca, Appl. Catal. B: Environ. 147 (2014) 813.
[50] K.S. Baamran, M. Tahir, M. Mohamed, A. Hussain Khoja, J. Environ. Chem. Eng. 8 (2020), 103604.
[51] T. Abbas, M. Tahir, Int. J. Hydrog. Energy 46 (2021) 8932.
[52] G. Vicente, J. Aguado, D. Serrano, N. Sánchez, J. Anal. Appl. Pyrolysis 85 (2009) 366.
[53] X. Zhang, H. Lei, G. Yadavalli, L. Zhu, Y. Wei, Y. Liu, Fuel 144 (2015) 33.
[54] D. Serrano, J. Aguado, J. Escola, J. Rodriguez, A. Peral, J. Catal. 276 (2010) 152.
[55] A. López, I. de Marco, B.M. Caballero, M.F. Laresgoiti, A. Adrados, A. Torres, Waste Manag. 31 (2011) 1973.
[56] R. Miandad, M. Rehan, M.A. Barakat, A.S. Aburiazaiza, H. Khan, I.M.I. Ismail, J. Dhavamani, J. Gardy, A. Hassanpour, A.-S. Nizami, Front. Energy Res. 7 (2019).
[57] M. Brebu, T. Tamminen, I. Spiridon, J. Anal. Appl. Pyrolysis 104 (2013) 531.
[58] W.-W. Liu, C.-W. Hu, Y. Yang, D.-M. Tong, L.-F. Zhu, R.-N. Zhang, B.-H. Zhao, Appl. Catal. B: Environ. 129 (2013) 202.
[59] F. Ateş, N. Miskolczi, N. Borsodi, Bioresour. Technol. 133 (2013) 443.
[60] L. Pino, C. Italiano, A. Vita, M. Laganà, V. Recupero, Appl. Catal. B: Environ. 218 (2017) 779.
[61] J. Guo, H. Lou, H. Zhao, D. Chai, X. Zheng, Appl. Catal. A: Gen. 273 (2004) 75.
[62] L. An, C. Dong, Y. Yang, J. Zhang, L. He, Renew. Energy 36 (2011) 930.